www.acsnano.org

# $Cr_xPt_{1-x}Te_2$ ( $x \le 0.45$ ): A Family of Air-Stable and Exfoliatable van der Waals Ferromagnets

Warren L. B. Huey, Andrew M. Ochs, Archibald J. Williams, Yuxin Zhang, Simo Kraguljac, Ziling Deng, Curtis E. Moore, Wolfgang Windl, Chun Ning Lau, and Joshua E. Goldberger\*



Cite This: ACS Nano 2022, 16, 3852-3860



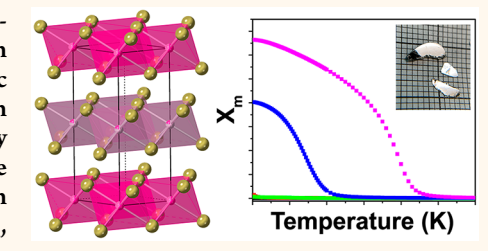
**ACCESS** I

Metrics & More

Article Recommendations

Supporting Information

ABSTRACT: The development of thermally robust, air-stable, exfoliatable two-dimensional van der Waals ferromagnetic materials with high transition temperatures is of great importance. Here, we establish a family of magnetic alloys,  $\operatorname{Cr}_x \operatorname{Pt}_{1-x} \operatorname{Te}_2$  ( $x \leq 0.45$ ), that combines the stability of the late transition metal dichalcogenide  $\operatorname{PtTe}_2$  with magnetism from Cr. These materials are easily grown in crystal form from the melt, are stable in ambient conditions, and have among the highest concentrations of magnetic element substitution in transition metal dichalcogenide alloys. The highest Cr-substituted material,  $\operatorname{Cr}_{0.45}\operatorname{Pt}_{0.55}\operatorname{Te}_2$ , exhibits ferromagnetic behavior below 220 K, and the easy axis is along the *c*-axis



of the material, as determined using a combination of neutron diffraction and magnetic susceptibility measurements. These materials are metallic, with appreciable magnetoresistance below the Curie temperature. Single-crystal and powder diffraction measurements indicate Cr readily alloys onto the Pt site and does not sit in the van der Waals space, allowing these materials to be readily exfoliated to the few-layer regime. In summary, this air-stable, exfoliatable, high transition temperature ferromagnet shows great potential as building block for future 2D devices.

KEYWORDS: 2D ferromagnetism, van der Waals materials, 2D material, layered material, ferromagnet

### INTRODUCTION

Downloaded via OHIO STATE UNIV on May 8, 2023 at 12:26:28 (UTC). See https://pubs.acs.org/sharingguidelines for options on how to legitimately share published articles.

The development of exfoliatable 2D van der Waals (vdW) materials with magnetic properties has attracted considerable interest ever since CrI<sub>3</sub> was shown to maintain ferromagnetism (FM) down to the monolayer limit. These 2D magnetic materials have offered the possibility to explore many intriguing phenomena, such as proximity effect induced magnetism, spin dynamics, and new moiré magnetic states, and have many potential applications in spintronics and as components in bulk heterostructures. However, many 2D van der Waals magnetic systems, such as the transition metal trihalides, suffer from extreme air and water sensitivity and low transition temperatures especially when exfoliated into the few-layer regime. A rigorous characterization of the atomic structure of monolayers whose properties are directly under investigation is rarely performed.

Together these difficulties can often result in a divergence of property measurements for the same materials. For instance, many chromium chalcogenide materials have received a lot of debate over their magnetic properties. One of the most recently studied 2D materials is metallic 1T-CrTe<sub>2</sub>. A number of synthesis methods have been used to make the material including the deintercalation of K from KCrTe<sub>2</sub>, <sup>16</sup> chemical vapor deposition (CVD), <sup>17</sup> and molecular beam epitaxy (MBE). <sup>18</sup> All three methods report ferromagnetism for 1T-CrTe<sub>2</sub> below 300 K. However, the easy axis of the material has

been reported in both the in-plane and cross-plane directions, while the stability of the material is poor, decomposing above >300 K and requiring a Te capping layer to protect it from oxidation when used in a heterostructure. 1T-CrSe<sub>2</sub> has been shown to be antiferromagnetic with a Néel temperature of ~165–180 K and is a metastable phase prepared *via*  $I_2$ -based deintercalation of KCrSe<sub>2</sub>. However, CrSe<sub>2</sub> monolayers grown on WSe<sub>2</sub> monolayers have been reported to be ferromagnetic, with a Curie temperature ( $T_C$ ) of 110 K, as a result of an increase in lattice constants and interlayer charge transfer. Additionally, CrGeTe<sub>3</sub>, or Cr<sub>2</sub>Ge<sub>2</sub>Te<sub>6</sub>, is another well explored 2D vdW system with soft ferromagnetism, a bulk  $T_C$  of 68 K, and a cross-plane easy axis. This  $T_C$  decreases to 30 K in the bilayer, which has been shown to be stable in air for 1.5 h before degradation begins.

Another family of 2D magnets that has attracted a lot of interest is the magnetically doped TMDs in which a magnetic element (V, Cr, Mn, Fe, Co, Ni) is substituted onto the TMD

Received: October 1, 2021 Accepted: February 9, 2022 Published: February 17, 2022





lattice. However, the maximum amount of magnetic element doping before phase separation is almost always ≤10%, which often puts them in the regime of dilute magnetic semiconductors. For instance, monolayers of MoS2 can be doped with ~2% Fe.<sup>21</sup> Additionally, ~3% Mn-doped MoS<sub>2</sub> shows ferromagnetism with a  $T_C$  of 350 K with a magnetic moment of 1.06  $\mu$ B/Mn.<sup>22</sup> The effects of magnetic doping of Co, Ni, Fe, and Mn (10%) on MoS<sub>2</sub> nanocrystals, Mn-doped (10%) MoSe<sub>2</sub>, and V-doped (12%) WS<sub>2</sub> or (9%) WSe<sub>2</sub> have also been explored. <sup>23–26</sup> Furthermore, while a handful of compounds such as MoS<sub>2</sub> and WS<sub>2</sub> are air-stable in both the bulk and monolayer form, most early transition metal tellurides have a strong propensity to oxidize, especially upon exfoliation, due to the thermodynamic driving force of metal oxide formation. It is a well-regarded principle in molecular inorganic chemistry that early transition metals tend to be much more oxophilic and prone toward oxidation than late transition metals.<sup>27</sup> Indeed, the late transition metal Pd and Pt TMDs have been shown to be air stable both in the bulk and in monolayer form.<sup>28–33</sup> Moreover, PtTe<sub>2</sub> has been claimed to be a type II Dirac semimetal, but these crossing points are energetically far removed from the Fermi level and thus do not cause any relevant exotic transport effects. 34,35

Herein, we show the preparation of an air- and water-stable series that merges the stability of a late transition metal dichalcogenide (PtTe<sub>2</sub>) with an early transition metal magnetic element. After an initial screening of transition metal alloys of V, Cr, Mn, and Ni with PtTe<sub>2</sub>, we found that Cr substitutes onto the Pt site, resulting in a van der Waals  $\text{Cr}_x\text{Pt}_{1-x}\text{Te}_2$  series with Cr concentrations reaching up to 45% before phase separation. These materials are ferromagnetic with  $\text{Cr}_{0.45}\text{Pt}_{0.55}\text{Te}_2$ , having a  $T_{\text{C}}$  of 220 K and an easy axis along the c-axis. The bulk material is metallic with appreciable magnetoresistance and can be exfoliated to few layer thicknesses.

## **RESULTS AND DISCUSSION**

The  $Cr_xPt_{1-x}Te_2$  series ( $0 \le x \le 0.45$ ) was synthesized from stoichiometric mixtures of the elements *via* traditional quartz tube reactions for the powders and from slow cooling of the melt for crystals. Figure 1 shows representative crystal structures of  $Cr_{0.21}Pt_{0.79}Te_2$  and  $Cr_{0.40}Pt_{0.60}Te_2$  as determined

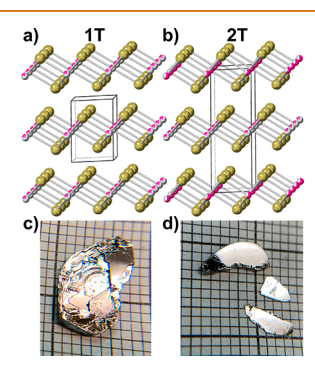


Figure 1. (a) Crystal structure of  $Cr_{0.21}Pt_{0.79}Te_2$  showing the  $P\overline{3}m1$  space group with a 1T unit cell. (b) Crystal structure of  $Cr_{0.40}Pt_{0.60}Te_2$  showing a 2T unit cell with one layer being Cr rich (60%) and the other being Cr poor (20%). In (a) and (b), Te is yellow, Pt is gray, and Cr is magenta. (c) Crystal of 1T PtTe<sub>2</sub> on mm-scale grid paper. (d) Crystals of 2T  $Cr_{0.40}Pt_{0.60}Te_2$  on mm-scale grid paper.

from single-crystal X-ray diffraction, as well as representative crystals of PtTe<sub>2</sub> and Cr<sub>0.40</sub>Pt<sub>0.60</sub>Te<sub>2</sub>. PtTe<sub>2</sub> crystallizes into a one-layer trigonal unit cell with a P3m1 space group. Singlecrystal XRD analysis indicates that this 1T P3m1 structure is maintained for x = 0.21 and x = 0.31, with the Cr atoms substituting onto the Pt position (Figure 1a). However, singlecrystal analysis of Cr<sub>0.40</sub>Pt<sub>0.60</sub>Te<sub>2</sub> indicated that it crystallized into a two-layer trigonal (2T) cell having a  $P\overline{3}m1$  space group. In this case, one layer of the new cell was found to be Cr rich ( $\sim$ 60%) and the other was Cr poor ( $\sim$ 20%) (Figure 1b). Although it is very common for metals to intercalate into van der Waals space of 2D transition metal dichalcogenides, 36 no Cr was found to occupy the octahedral or tetrahedral holes in the van der Waals space. This confirms that Cr is alloying onto the Pt site and not intercalating. In addition, large, well-faceted crystals having dimensions of >5 mm × 5 mm and thicknesses of ~1 mm can be readily prepared from the melt across the entire series, as shown for PtTe<sub>2</sub> and Cr<sub>0.40</sub>Pt<sub>0.60</sub>Te<sub>2</sub> (Figure 1c and d). Single-crystalline domains can be extracted from the solidified ingot, through mechanical exfoliation. The Cr:Pt stoichiometries in these extracted single crystals of  $Cr_xPt_{1-x}Te_2$ can vary by x = 0.05 in a particular batch, based on singlecrystal XRD.

Powder diffraction in combination with Rietveld analysis was used to establish the changes in the structure that occur with increasing Cr alloying (Tables S1-S12). A uniform change in the lattice parameters is observed in the XRD patterns across the series (Figure 2a and b). In addition, the transformation from the 1T polytype ( $x \le 0.35$ ) to the 2T polytype (x = 0.45) is apparent based on the emergence of a new 001 peak at  $8^{\circ}$  2 $\theta$ in Cr<sub>0.45</sub>Pt<sub>0.55</sub>Te<sub>2</sub>. With increasing Cr content, the interlayer spacing increases from 5.224 Å to 5.490 Å, whereas the inplane a lattice parameter uniformly decreases from 4.025 Å to 3.965 Å (Figure 2c). Overall, the unit cell volume per layer increases from 73.294 Å<sup>3</sup> to 74.732 Å<sup>3</sup> with increasing Cr content (Figure 2d). The uniform changes in lattice constants and volume indicate a homogeneous alloy up to 45% Cr substitution. Synthetic attempts with Cr substitution above 45% resulted in the emergence of a Cr<sub>2</sub>Te<sub>3</sub> impurity phase. Next, Rietveld analysis of the Cr<sub>x</sub>Pt<sub>1-x</sub>Te<sub>2</sub> powders produced a much better fit when Cr was alloyed onto the Pt site rather than intercalated onto the octahedral or tetrahedral hole in the van der Waals space. This matches the single-crystal diffraction analysis and further confirms the absence of Cr intercalation. In all powder patterns with x < 0.45, no reflections of other  $Cr_xTe_y$  phases were observed, including  $Cr_xTe_3^{,37}$   $CrTe_3^{,38}$   $Cr_2Te_3^{,39}$  and  $Cr_5Te_8^{,40-42}$  Occasionally very weak reflections corresponding to excess Te were observed. Finally, all samples can be stored in air and light for at least eight months without any changes in the observed diffraction pattern.

The magnetic properties of the  $Cr_xPt_{1-x}Te_2$  compounds were investigated via SQUID magnetometry. The 500 Oe field cooled (FC) magnetic susceptibility of powders from 2 to 300 K are shown in Figures 3a and S1. PtTe<sub>2</sub> was previously reported to have an overall tiny and slightly negative diamagnetic mass susceptibility ( $-5 \times 10^{-8}$  cm<sup>3</sup> g<sup>-1</sup> at 90 K), which we confirm here ( $-17 \times 10^{-8}$  cm<sup>3</sup> g<sup>-1</sup> at 90 K). Alloying even a small amount of Cr into the PtTe<sub>2</sub> phase leads to a significant increase in magnetic susceptibility. Furthermore, incorporating greater amounts of Cr leads to an increase in both the molar susceptibility and the magnetic transition temperature of the material. Herein, we define  $T_C$  as the inflection point based on the second derivative of the magnetic

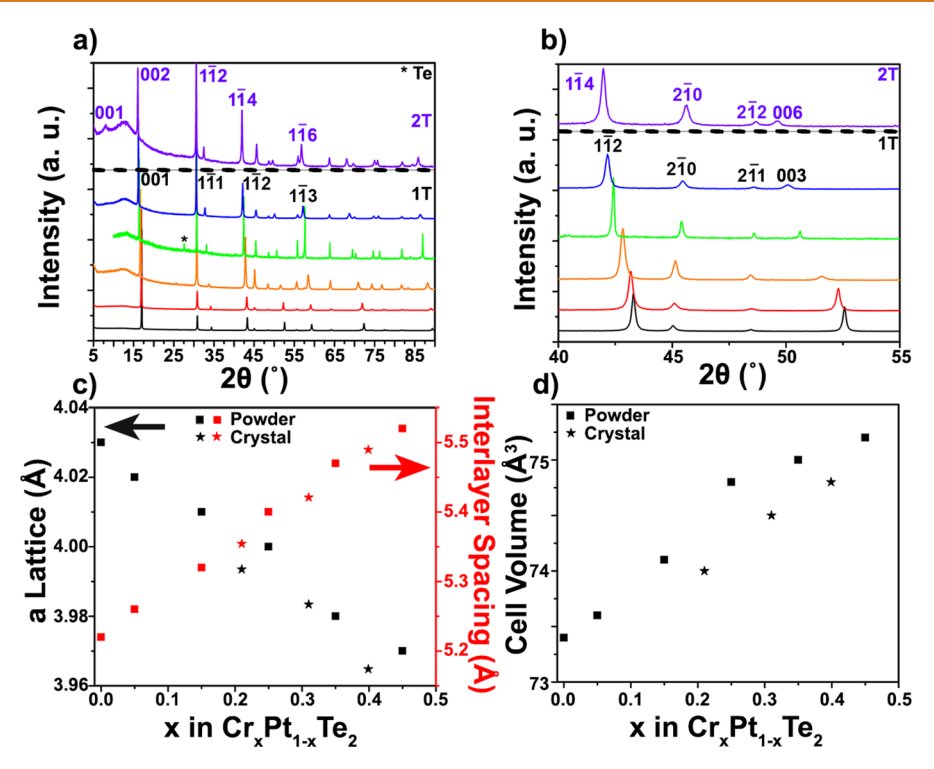


Figure 2. (a) Powder XRD patterns of PtTe<sub>2</sub> (black), Cr<sub>0.05</sub>Pt<sub>0.95</sub>Te<sub>2</sub> (red), Cr<sub>0.15</sub>Pt<sub>0.85</sub>Te<sub>2</sub> (orange), Cr<sub>0.25</sub>Pt<sub>0.75</sub>Te<sub>2</sub> (green), Cr<sub>0.35</sub>Pt<sub>0.65</sub>Te<sub>2</sub> (blue), and Cr<sub>0.45</sub>Pt<sub>0.55</sub>Te<sub>2</sub> (purple) showing major peak labels and shifts from 1T (below dotted line) to 2T (above dotted line). The starred peak in the Cr<sub>0.25</sub>Pt<sub>0.75</sub>Te<sub>2</sub> spectrum corresponds to the most intense Te reflection. (b) Zoom-in of the 40–55° 2θ region highlighting the uniform change in lattice parameters with greater Cr concentration. (c) Changes in a lattice constant (black, left) and interlayer spacing (red, right) with Cr content for Cr<sub>x</sub>Pt<sub>1-x</sub>Te<sub>2</sub> powders (squares) and crystals (stars). (d) Changes in cell volume, normalized per layer, with Cr content for Cr<sub>x</sub>Pt<sub>1-x</sub>Te<sub>2</sub> as determined from powder diffraction (squares) and single-crystal diffraction (stars). The error in the (c) lattice parameters and (d) cell volume, as determined *via* refinements, is smaller than the data points.

susceptibility. With  $Cr_{0.25}Pt_{0.75}Te_2$  the Curie temperature occurs at 48 K (Figure S1).  $Cr_{0.35}Pt_{0.65}Te_2$  and  $Cr_{0.45}Pt_{0.55}Te_2$ show ferromagnetic transitions at 105 and 220 K, respectively (Figure S2). The 2 K M vs H plots confirm the ferromagnetic behavior in Cr<sub>0.35</sub>Pt<sub>0.65</sub>Te<sub>2</sub> and Cr<sub>0.45</sub>Pt<sub>0.65</sub>Te<sub>2</sub> due to the presence of hysteresis (Figure 3b). Cr<sub>0.35</sub>Pt<sub>0.65</sub>Te<sub>2</sub> is a hard ferromagnetic material with a coercive field of 0.40 T and saturation magnetization of 1.62  $\mu_{\rm B}/{\rm Cr}$  atom. For Cr<sub>0.45</sub>Pt<sub>0.55</sub>Te<sub>2</sub>, the saturation magnetization increases to 2.25  $\mu_{\rm B}/{\rm Cr}$  atom, while, surprisingly, the coercive field decreases to ~0.10 T. This reduction in coercive field in the Cr<sub>0.45</sub>Pt<sub>0.55</sub>Te<sub>2</sub> phase is likely a consequence of the alternatingly Cr-rich and -poor layers in the 2T polytype, which will result in a reduced interlayer magnetic coupling compared to the 1T polytype Cr<sub>0.35</sub>Pt<sub>0.65</sub>Te<sub>2</sub>, which features evenly distributed Cr. It is also interesting to note that the magnetic susceptibility and magnetization saturation moment per Cr decreases from Cr<sub>0.05</sub>Pt<sub>0.95</sub>Te<sub>2</sub> to Cr<sub>0.25</sub>Pt<sub>0.75</sub>Te<sub>2</sub>, before increasing appreciably. It has been well established that in dilute magnetic metals the magnetic coupling can oscillate based on the separation distance of magnetic elements (such as in a Ruderman-Kittel-Kasuya-Yosida mechanism), which we suspect occurs here as well, but will be the subject of future inquiry.

We then investigated the magnetic properties of single crystals of  $Cr_{0.45}Pt_{0.55}Te_2$  in detail. The 500 Oe FC and zero-field cooled (ZFC) magnetic susceptibility measured with the 500 Oe measurement field applied along the in-plane and cross-plane directions are shown in Figure 3c. When the field is applied along the in-plane direction, the ZFC and FC curves are nearly superimposable. However, when the field is applied

along the cross-plane direction, a significant deviation between the ZFC and FC curves is apparent. The cross-plane and inplane orientations of the single crystal both had a  $T_{\rm C}$  of ~191 K, which is relatively close to the Weiss constant  $(\Theta)$  of ~211 K obtained from the Curie—Weiss fitting (Figure S3). The inplane and cross-plane M vs H plot is shown in Figure 3d. When the field is applied along the cross-plane direction, there is an appreciable hysteresis with a coercive field of 0.17 T, and the magnetization saturates to  $\sim 2.37 \mu_B/Cr$  atom at a much lower applied field. Thus, the cross-plane direction is the easy axis and the direction of spin alignment. The unusual difference between the FC and ZFC susceptibility along the cross-plane direction in Figure 3c arises from the fact that the measurement field is smaller than the coercive field. Finally, the 2.25–2.37  $\mu_{\rm B}/{\rm Cr}$  is relatively close to the expected spinonly moment of a  $Cr^{4+}$   $d^2$  spin system, which would be 2.8  $\mu_B$ / Cr. The assignment of a formal oxidation state to Cr is complicated by the metallic nature of this compound, for which the delocalization of electrons often leads to a reduced magnetic moment. Also, further confirmation of the chromium oxidation state using X-ray photoelectron spectroscopy is confounded from the spectral overlap between the Cr 2p and Te 3d peaks. In order to shed additional light on this question, the magnetic moment per Cr atom was examined with density functional theory (DFT) for an ideal defect-free sample at zero temperature. DFT finds a magnetic moment of 2.72  $\mu$ B/Cr, giving strong support to the hypothesis of a Cr4+ d2 spin system where the expectation is 2.8  $\mu$ B/Cr. The origin of the magnetization from the Cr d-states can be clearly seen in the spin-resolved density of states in Figure 4.

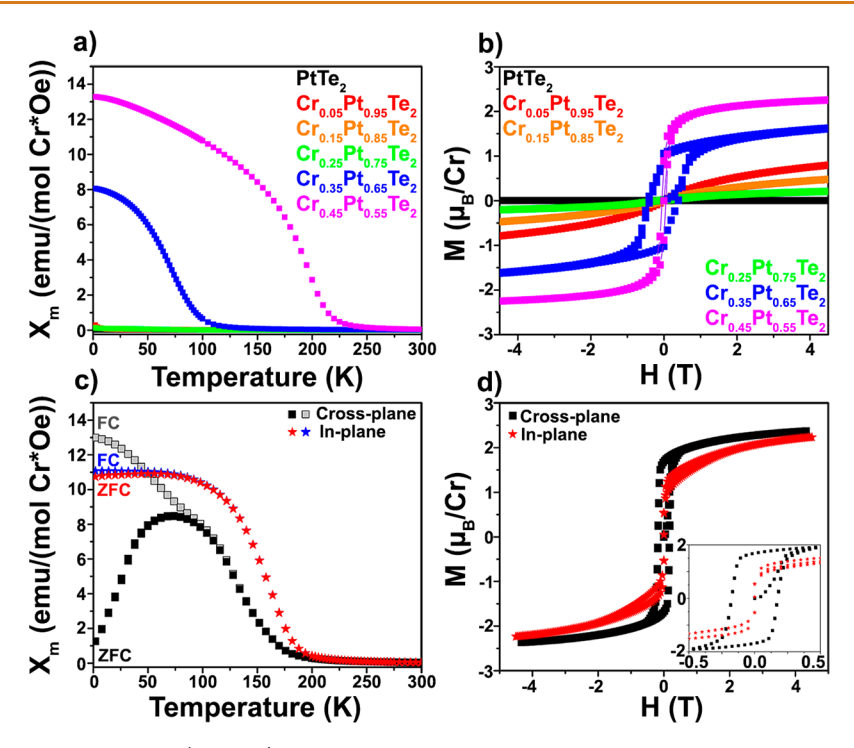


Figure 3. (a) Temperature-dependent FC (500 Oe) magnetic molar susceptibility for the powder  $Cr_xPt_{1-x}Te_2$  series, using a 500 Oe measurement field. The susceptibility was normalized to moles Cr, except for  $PtTe_2$ , which was normalized to moles Pt. (b) Field-dependent magnetization at 2 K for the powder  $Cr_xPt_{1-x}Te_2$  series. The magnetization in  $\mu_B$  was normalized per Cr atom, except Cr which was normalized per Cr atom, except Cr which was normalized per Cr atom, except Cr which was normalized per Cr atom, except Cr atom, except Cr which was normalized per Cr atom, except Cr atom, except Cr which was normalized per Cr atom, except Cr atom, except Cr which was normalized per Cr atom, except Cr atom, except

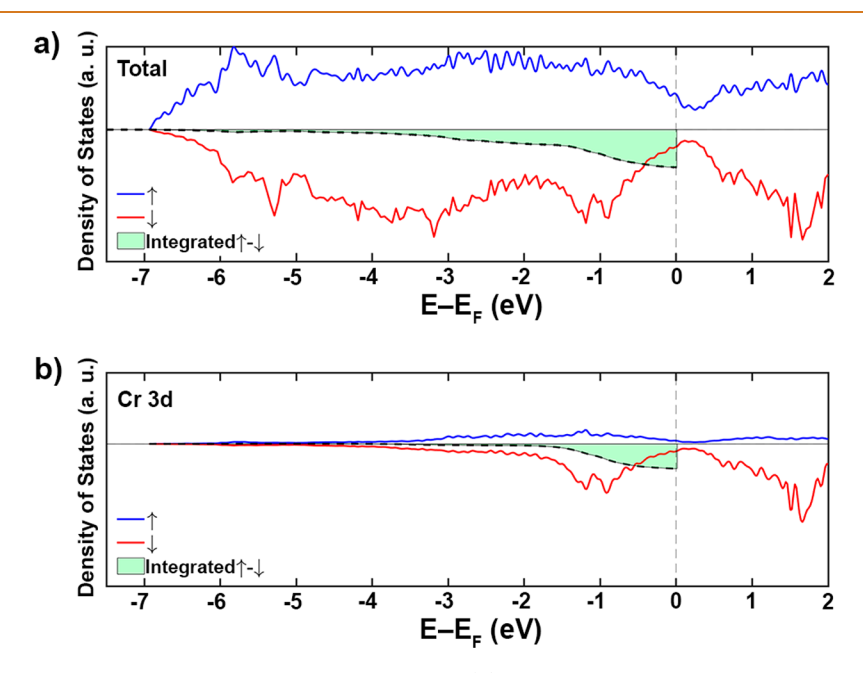


Figure 4. (a) Spin-resolved DOS of  $Cr_{0.45}Pt_{0.55}Te_2$  for all orbitals and (b) for just the Cr 3d orbitals. The region highlighted in green corresponds to the integrated total magnetization with increasing energy, highlighting that it is the Cr 3d orbitals  $\sim$ 1 eV below the Fermi level that are primarily responsible for the overall magnetization.

To further elucidate the magnetic structure of  $Cr_{0.45}Pt_{0.55}Te_2$ , time-of-flight neutron powder diffraction data were collected above  $T_{\rm C}$  at 250 K as well as below  $T_{\rm C}$  at 100 and 10 K (Figure 5). No new reflections indicative of

antiferromagnetism were apparent in the 100 and 10 K data sets. In addition, certain reflections gained in intensity upon cooling, indicative of ferromagnetism. Considering the 1a and 1b Wyckoff positions of the Cr atoms in the  $2T P\overline{3}m1$ 

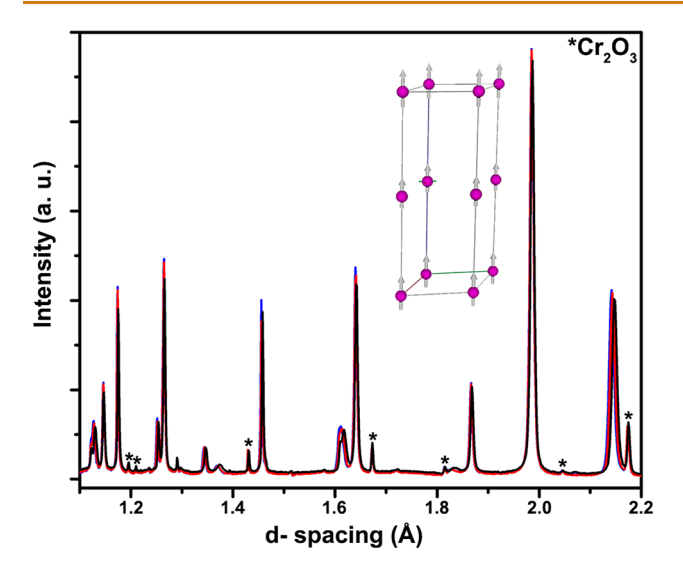


Figure 5. High-resolution powder neutron diffraction spectrum using frame 3 of POWGEN at ORNL showing a magnetic contribution from  $Cr_{0.45}Pt_{0.55}Te_2$  at 250 K (black), 100 K (red), and 10 K (blue). The inset shows the magnetic moment of the Cr atoms in the structure at 10 K. Starred peaks correspond to the trace 3% phase fraction  $Cr_2O_3$  impurity.

crystallographic phases, respectively, only the P3m'1 magnetic group can lead to ferromagnetic order. This magnetic group requires the Cr spins to be oriented along the c-axis. Rietveld analysis was performed on each data set, and a ferromagnetic structure was required for the 100 and 10 K data sets to achieve a good fit. At 100 and 10 K, the Cr atoms in the Crrich layer had a magnetic moment of 1.0(5) and 1.6(3)  $\mu_B/Cr$ atom, respectively, whereas the Cr-poor layers had 0.8(7) and 1.3(5)  $\mu_{\rm B}/{\rm Cr}$  atom, respectively. The 10 K magnetic structure is shown in Figure 5, inset. It is important to point out that a trace (~3% phase fraction based on neutron Rietveld analysis) Cr<sub>2</sub>O<sub>3</sub> impurity formed in this large-scale synthesis of powder, as evidenced by both in-house lab X-ray and neutron diffraction. The low intensity and minimal overlap of the Cr<sub>2</sub>O<sub>3</sub> reflections did not affect the fitting of the Cr<sub>0.45</sub>Pt<sub>0.55</sub>Te<sub>2</sub> phase in the neutron diffraction, especially since Cr<sub>2</sub>O<sub>3</sub> is an antiferromagnet with a Néel temperature of 308 K.4

A Rhodes-Wohlfarth ratio (RWR) analysis was used to characterize the amount of delocalization of the magnetic moment within the material.<sup>44</sup> RWR =  $P_c/P_s$  where  $P_c$  is the magnetic moment calculated from  $P_c(P_c + 2) = P_{eff}^2$  is taken from the susceptibility of the paramagnetic phase via a high-temperature Curie-Weiss fitting. P<sub>s</sub> is the saturation magnetic moment collected from the M vs H plots below the transition temperature of the material.<sup>45</sup> When RWR = 1, the P<sub>c</sub> and P<sub>s</sub> values are equal, indicating localized magnetic moments. However, when RWR > 1, this indicates that the magnetic moments are from electrons that are itinerant. 46,47 The  $P_c$  value was determined to be 4.18  $\mu$ B/Cr from the Cr<sub>0.45</sub>Pt<sub>0.55</sub>Te<sub>2</sub> cross-plane FC Curie-Weiss plot, while the P<sub>s</sub> value of 2.37  $\mu$ B/Cr was taken from the Cr<sub>0.45</sub>Pt<sub>0.55</sub>Te<sub>2</sub> crossplane magnetization curve at 2 K. The calculated RWR of 1.76 suggests that the magnetic moments in  $Cr_{0.45}Pt_{0.55}Te_2$  are from itinerant electrons.

We then investigated the changes in Raman spectra as Cr is alloyed onto the lattice, since Raman spectroscopy has been established as one of the most powerful characterization techniques for 2D materials. In all compounds two major

Raman modes are observed, one at 110–125 cm<sup>-1</sup> and a second at 150–160 cm<sup>-1</sup> (Figure 6a). Generally, as more Cr is

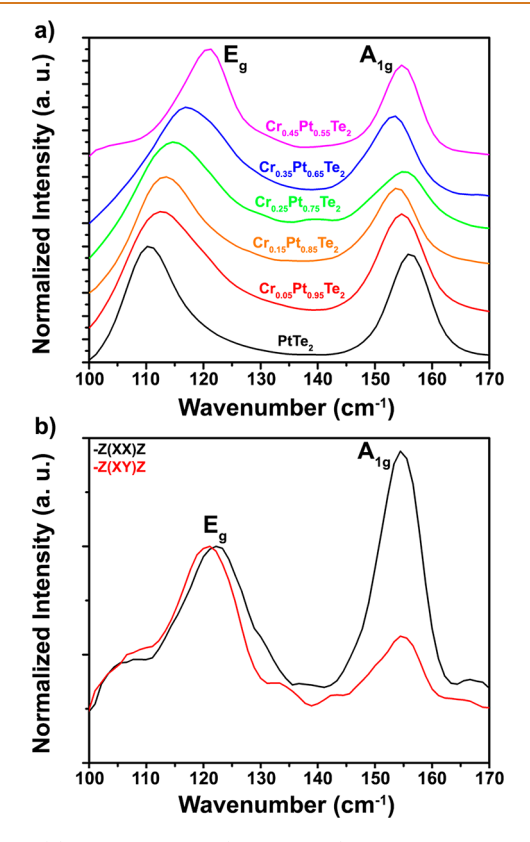


Figure 6. (a) Raman spectra ( $\lambda$  = 633 nm) of the  $Cr_xPt_{1-x}Te_2$  series showing shifts in the  $E_g$  and  $A_{1g}$  peaks with increasing Cr content. (b) Polarized Raman spectra of  $Cr_{0.45}Pt_{0.55}Te_2$  showing the change in the  $A_{1g}$  peak as the light is polarized in the -Z(XX)Z and -Z(XY)Z orientations.

alloyed onto the PtTe2 lattice, the decrease in reduced mass causes these Raman modes to shift to higher frequencies. To further confirm the symmetry of these modes, polarized Raman spectroscopy was performed looking down the c-axis in backscattering geometry. Both the 1T and 2T phases belong to the P3m1 space group, in which the Te atoms occupy the 2d Wyckoff positions that have local  $C_{3\nu}$  symmetry. Consequently, the 1T phases will have two Raman-active modes: one A<sub>1g</sub> and one E<sub>g</sub> mode. The 2T phases will have four Raman-active modes: two A<sub>1g</sub> and two E<sub>g</sub> modes. In the 2T phase, the Crrich and Cr-poor layers have very similar local structures. Thus, the two  $A_{1g}$  modes will likely occur at similar energies, as will the two  $E_g$  modes. The  $A_{1g}$  and  $E_g$  modes are both expected to appear when the polarized filter is parallel to the polarization of the light source, i.e., -Z(XX)Z configuration in Porto's notation. When the polarized filter is perpendicular to the polarization of the light source, or -Z(XY)Z configuration, only the E<sub>o</sub> modes are expected to be visible. In the polarized Raman spectra of  $Cr_{0.45}Pt_{0.55}Te_2$  (Figure 6b), the intensity of the Raman mode at  $\sim 155~\text{cm}^{-1}$  significantly decreases in crosspolarization, confirming that it has  $A_{1g}$  symmetry. It is important to note the absence of additional Raman peaks in the range of 100-200 cm<sup>-1</sup>, which would be indicative of TeO2, further showing the resilience of these systems against oxidation.49

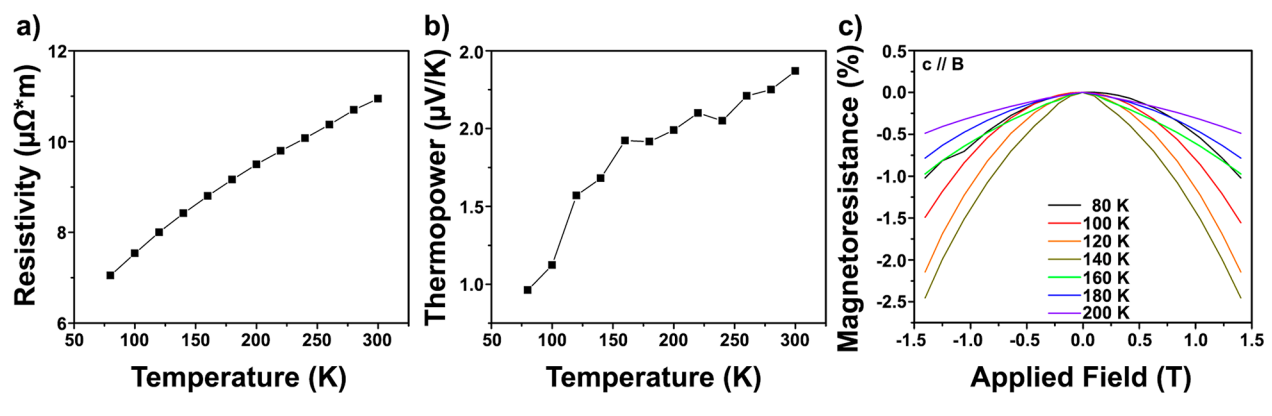


Figure 7. (a) In-plane electrical resistivity and (b) in-plane thermopower of  $Cr_{0.45}Pt_{0.55}Te_2$  from 80 to 300 K. (c) Percent in-plane magnetoresistance of  $Cr_{0.45}Pt_{0.55}Te_2$  from 80 to 200 K with applied field oriented along the cross-plane direction.

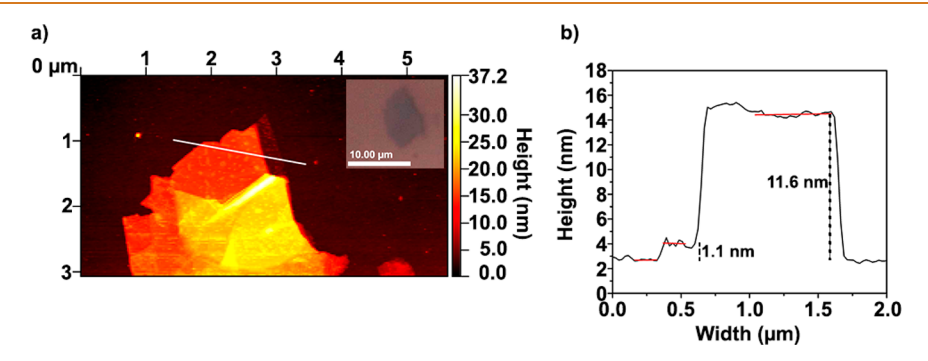


Figure 8. (a) AFM imaging of Cr<sub>0.45</sub>Pt<sub>0.55</sub>Te<sub>2</sub> showing the height profile of an indicated region and inset showing an optical image of the measured flake. (b) Height profile from (a) showing a bilayer portion of the thicker flake.

As previous studies have found 1T-PtTe2 to be metallic, four-probe in-plane resistivity measurements were collected on Cr<sub>0.45</sub>Pt<sub>0.55</sub>Te<sub>2</sub> from 300 to 80 K, to determine the influence of Cr alloying on the electronic properties. The resistivities are very low and increase from 7  $\mu\Omega$  m at 80 K to 11  $\mu\Omega$  m at 300 K, indicative of metallic behavior (Figure 7a) as expected from the DOS (Figure 4). The measured thermopowers are also quite small, as would be expected for metallic materials, and vary from 0.9 to 2.4  $\mu$ V K<sup>-1</sup> from 80 to 300 K (Figure 7b). It is well established that the resistance of ferromagnetic metals decreases when a field is applied due to the suppression of spin fluctuations throughout the material. Indeed, below  $T_C$ , a negative magnetoresistance of 2.5% was observed when a magnetic field was applied along the easy axis (Figure 7c). The magnetoresistance has a quadratic dependence with respect to the applied cross-plane magnetic field.

Finally, to demonstrate the possibility of accessing few to single layers, bulk single crystals of  $Cr_{0.45}Pt_{0.55}Te_2$  were mechanically exfoliated onto 285 nm  $SiO_2/Si$  substrates using Kapton tape. From this technique, regions with thicknesses of ~10 nm are readily prepared and visible *via* optical microscopy (Figure 8a inset). Furthermore, regions down to 1.1 nm were observed near thicker flakes, which corresponds to a thickness of two van der Waals layers (Figure 8a and b). In contrast to many other magnetic phases that exhibit extreme air-sensitivity such as  $CrI_3$ , there are no apparent changes in optical microscopy or AFM measurements indicative of oxidation, such as hole formation, or increases in surface roughness, despite exposure to air for eight months (Figure S4). Future studies of the properties of exfoliated

monolayer and bilayers should provide further verification of the resistance against oxidation.

# CONCLUSIONS

We have developed a family of exfoliatable, 2D van der Waals metallic ferromagnets,  $\mathrm{Cr_xPt_{1-x}Te_2}$ , that marries the stability of the late transition metal Pt with magnetism from Cr. These compounds are readily synthesized in single-crystal form, simply from cooling the melt, further underlining its thermodynamic stability. It is possible to substitute up to 45% of the Pt in  $\mathrm{PtTe_2}$  with Cr, allowing for a robust high transition temperature ( $T_{\rm C} = 220~{\rm K}$ ) ferromagnet that, despite eight months of air exposure, shows minimal degradation or changes in properties. This stable 2D ferromagnet is an exciting building block for future explorations in spintronic and magnetoelectronic properties and devices.

# **EXPERIMENTAL METHODS**

**Synthesis Methods.** Polycrystalline powders and crystals of  $Cr_xPt_{1-x}Te_2$  ( $x \le 0.45$ ) were synthesized from the elements. Due to the air reactivity of Cr at higher temperatures, stoichiometric amounts of the elemental powders of Cr (99.99%, Alfa Aesar) and Pt (99.98%, Alfa Aesar) with Te pieces (99.999%, Aldrich) were added to a quartz crucible and sealed in a larger quartz tube under a  $\le 70$  mTorr Ar atmosphere. To produce powdered  $Cr_xPt_{1-x}Te_2$ , the elements were heated to 800 °C over 3 h, held at temperature for a week, and allowed to cool to room temperature over 60 h. To produce single crystals of  $Cr_xPt_{1-x}Te_2$  from the melt, the elements were heated to 1100 °C over 3 h, held at temperature for 24 h, and let cool to 700 °C at 2 °C/h and air cool below 700 °C to room temperature. Single crystals can be extracted from the ingot *via* mechanical exfoliation. Single crystals of  $PtTe_2$  were grown *via* Te flux with a 1:17 Pt to Te ratio. Pt powder and Te pieces were placed in a quartz crucible inside

a large quartz tube with quartz wool placed above the crucible and sealed under a  ${\leq}60$  mTorr Ar atmosphere. The material was heated to 1000 °C over 4 h, held at temperature for 8 h, and then cooled at 2 °C/h to 500 °C. At 500 °C, the tube was removed from the furnace, inverted, and centrifuged at 1000 rpm for 10 min to remove excess Te.

**Characterization Methods.** After synthesis, all samples were handled and stored in air. A Bruker D8 Advance powder X-ray diffractometer, with Cu K $\alpha$  radiation, was used to collected X-ray diffraction (XRD) patterns for the  $Cr_xPt_{1-x}Te_2$  powder series.

The single-crystal X-ray diffraction studies were carried out on a Nonius Kappa diffractometer equipped with a Bruker APEX-II CCD and Mo K $\alpha$  radiation ( $\lambda$  = 0.710 73 Å). A 0.071 × 0.055 × 0.052 mm piece of a metallic silver block was mounted on a cryoloop with clear enamel. Data were collected at ambient conditions using  $\phi$  and  $\varpi$ scans. The crystal-to-detector distance was 40 mm and the exposure time was 5 s per frame using a scan width of 2.0°. Data collection was 100% complete to 25.00° in  $\theta$ . A total of 3749 reflections were collected covering the indices  $-5 < = h \le 5, -5 \le k \le 5, -7 \le l \le 7$ . A total of 109 reflections were found to be symmetry independent, with an  $R_{\rm int}$  of 0.0491. Indexing and unit cell refinement indicated a primitive, trigonal lattice. The space group was found to be  $P\overline{3}m1$ . The data were integrated using the Bruker SAINT software program and scaled using the SADABS software program. Solution by direct methods (SHELXT) produced a complete phasing model for refinement. All atoms were refined anisotropically by full-matrix least-squares (SHELXL-2014).

A Quantum Design MPMS3 superconducting quantum interference device (SQUID) magnetometer was used to measure the molar magnetic susceptibility and magnetization of the powder and singlecrystal Cr<sub>x</sub>Pt<sub>1-x</sub>Te<sub>2</sub> series. The powder series (~50-100 mg) was placed in a gelatin capsule, sealed with Kapton tape, and inserted into a straw for SQUID measurements. Single crystals were enclosed between two pieces of Kapton tape and attached inside the straw via a cutout with Kapton tape for both in-plane and cross-plane orientation measurements. For M vs H plots, the magnetization data were collected at 2 K by cooling the material to temperature and then sweeping the applied field from 0 T up to 4.5 T, down to −4.5 T, and back to 4.5 T. To account for the demagnetization factor when measuring along the cross-plane direction, a correction factor was applied to the external field using  $H_i = H_e - NM$  where  $H_i$  is the intrinsic field,  $H_e$  is the applied external field, N is the shape factor (which is equal to  $4\pi$  for a sheet that is perpendicular to  $H_e$ ), and M is the measured magnetization.

DFT calculations were performed on a 2  $\times$  5  $\times$  1 60-atom  $Cr_{0.45}Pt_{0.55}Te_2$  2T supercell generated by the mcsqs code of the Alloy Theoretic Automated Toolkit (ATAT)<sup>50</sup> as a special quasi-random structure (SQS)<sup>51</sup> with different Cr concentrations in the two layers as measured. The structure was relaxed, and electron density of states (DOS) and magnetization were calculated with the Vienna *ab initio* Simulation Package (VASP)<sup>52</sup> using the plane wave projector augmented-wave (PAW) method<sup>53</sup> and the PBE<sup>54</sup> functional, together with van der Waals corrections. <sup>55,56</sup> The Brillouin zone was sampled on a 4  $\times$  4  $\times$  4  $\times$  4-point grid, and a plane-wave energy cutoff of 400 eV was used.

Time-of-flight neutron diffraction on powders was collected using the POWGEN beamline at Oak Ridge National Laboratory. Frames 1 and 3 were collected and utilized to characterize the magnetic structure of  $Cr_{0.45}Pt_{0.55}Te_2$  at 250, 100, and 10 K.

Raman scattering spectra were collected using a Renishaw Raman IR microprobe with an inVia confocal Raman microscope, with a 633 nm laser light source and a charge-coupled detector. For polarized Raman measurements, a Pike Technologies KRS-5 polarizer was placed before the charge-coupled detector.

Four-probe temperature-dependent in-plane resistivity and thermopower measurements were performed simultaneously on a single crystal of  $\operatorname{Cr}_x\operatorname{Pt}_{1-x}\operatorname{Te}_2$  using a home-built setup in a liquid  $\operatorname{N}_2$  cryostat. A small brass sheet was attached to the top of the crystal underneath a resistance heater, and a second brass sheet was attached to the bottom of the crystal and connected to an alumina heat sink. Copper—

constantan thermocouples were attached at two points along the crystal with Ag epoxy to measure the temperature gradient. The copper legs of the thermocouples were also used to measure the thermopower voltage. For resistivity measurements, current was applied through the top and bottom brass sheets, while the copper legs were used to measure the voltage. The same setup was also used for magnetoresistance measurements, but with an applied magnetic field ranging from  $\pm 1.4~{\rm T}$  in the cross-plane direction.

Atomic force microscopy measurements were performed on exfoliated flakes of  $Cr_{0.45}Pt_{0.55}Te_2$  that were prepared via Kapton tape exfoliation onto 285 nm  $SiO_2/Si$  substrates. A Bruker AXS Dimension Icon atomic/magnetic force microscope with ScanAsyst was used for thickness and few-layer stability measurements.

#### **ASSOCIATED CONTENT**

# Supporting Information

CIF files showing the The Supporting Information is available free of charge at https://pubs.acs.org/doi/10.1021/acsnano.1c08681.

Rietveld refinements of powder  $Cr_xPt_{1-x}Te_2$  using GSAS2, temperature-dependent FC magnetic molar susceptibility of powder  $Cr_xPt_{1-x}Te_2$ , Curie—Weiss fitting of  $Cr_{0.45}Pt_{0.55}Te_2$  and  $Cr_{0.35}Pt_{0.65}Te_2$  powder, and Curie—Weiss fitting of single-crystal  $Cr_{0.45}Pt_{0.55}Te_2$  in both the in-plane and cross-plane directions; AFM images of exfoliated few-layer flakes before and after 8 months' air exposure (PDF)

Single-crystal structure of Cr<sub>0.21</sub>Pt<sub>0.79</sub>Te<sub>2</sub> (CIF)

Single-crystal structure of Cr<sub>0.31</sub>Pt<sub>0.69</sub>Te<sub>2</sub> (CIF)

Single-crystal structure of Cr<sub>0.40</sub>Pt<sub>0.60</sub>Te<sub>2</sub> (CIF)

#### **AUTHOR INFORMATION**

## **Corresponding Author**

Joshua E. Goldberger — Department of Chemistry and Biochemistry, The Ohio State University, Columbus, Ohio 43210, United States; orcid.org/0000-0003-4284-604X; Email: goldberger.4@osu.edu

#### **Authors**

Warren L. B. Huey – Department of Chemistry and Biochemistry, The Ohio State University, Columbus, Ohio 43210, United States

Andrew M. Ochs – Department of Chemistry and Biochemistry, The Ohio State University, Columbus, Ohio 43210, United States

Archibald J. Williams – Department of Chemistry and Biochemistry, The Ohio State University, Columbus, Ohio 43210, United States

Yuxin Zhang — Department of Physics, The Ohio State University, Columbus, Ohio 43210, United States

Simo Kraguljac – Department of Chemistry and Biochemistry, The Ohio State University, Columbus, Ohio 43210, United States

Ziling Deng — Department of Materials Science and Engineering, The Ohio State University, Columbus, Ohio 43210, United States

Curtis E. Moore — Department of Chemistry and Biochemistry, The Ohio State University, Columbus, Ohio 43210, United States; © orcid.org/0000-0002-3311-7155

Wolfgang Windl – Department of Materials Science and Engineering, The Ohio State University, Columbus, Ohio 43210, United States Chun Ning Lau — Department of Physics, The Ohio State University, Columbus, Ohio 43210, United States; orcid.org/0000-0003-2159-6723

Complete contact information is available at: https://pubs.acs.org/10.1021/acsnano.1c08681

#### **Author Contributions**

The manuscript was written through contributions of all authors. All authors have given approval to the final version of the manuscript.

#### Notes

The authors declare no competing financial interest.

## **ACKNOWLEDGMENTS**

This research was primarily supported by the Center for Emergent Materials, an NSF MRSEC, under award number DMR-2011876. A portion of this research used resources at the Spallation Neutron Source, a DOE Office of Science User Facility operated by the Oak Ridge National Laboratory. Y.Z. and C.N.L. acknowledge the support of DMR 2004801. Z.D. and W.W. acknowledge funding by AFOSR, Award FA9550-21-1-0268, program director Dr. Ali Sayir, and supercomputing resources from the Ohio Supercomputer Center under project number PA0072.

#### **REFERENCES**

- (1) Huang, B.; Clark, G.; Navarro-Moratalla, E.; Klein, D. R.; Cheng, R.; Seyler, K. L.; Zhong, D.; Schmidgall, E.; McGuire, M. A.; Cobden, D. H.; Yao, W.; Xiao, D.; Jarillo-Herrero, P.; Xu, X. Layer-Dependent Ferromagnetism in a van der Waals Crystal Down to the Monolayer Limit. *Nature* **2017**, *546* (7657), 270–273.
- (2) Avsar, A.; Tan, J. Y.; Taychatanapat, T.; Balakrishnan, J.; Koon, G. K. W.; Yeo, Y.; Lahiri, J.; Carvalho, A.; Rodin, A. S.; O'Farrell, E. C. T.; Eda, G.; Castro Neto, A. H.; Özyilmaz, B. Spin—Orbit Proximity Effect in Graphene. *Nat. Commun.* **2014**, *5* (1), 4875.
- (3) Zhang, X.-X.; Li, L.; Weber, D.; Goldberger, J.; Mak, K. F.; Shan, J. Gate-Tunable Spin Waves in Antiferromagnetic Atomic Bilayers. *Nat. Mater.* **2020**, *19* (8), 838–842.
- (4) Li, T.; Jiang, S.; Sivadas, N.; Wang, Z.; Xu, Y.; Weber, D.; Goldberger, J. E.; Watanabe, K.; Taniguchi, T.; Fennie, C. J.; Fai Mak, K.; Shan, J. Pressure-Controlled Interlayer Magnetism in Atomically Thin CrI3. *Nat. Mater.* **2019**, *18* (12), 1303–1308.
- (5) Bistritzer, R.; MacDonald, A. H. Moiré Bands in Twisted Double-Layer Graphene. *Proc. Natl. Acad. Sci. U. S. A.* **2011**, *108* (30), 12233
- (6) Gong, C.; Li, L.; Li, Z.; Ji, H.; Stern, A.; Xia, Y.; Cao, T.; Bao, W.; Wang, C.; Wang, Y.; Qiu, Z. Q.; Cava, R. J.; Louie, S. G.; Xia, J.; Zhang, X. Discovery of Intrinsic Ferromagnetism in Two-Dimensional van der Waals Crystals. *Nature* **2017**, *546* (7657), 265–269.
- (7) Han, W.; Kawakami, R. K.; Gmitra, M.; Fabian, J. Graphene Spintronics. *Nat. Nanotechnol.* **2014**, *9* (10), 794–807.
- (8) Chang, C.-Z.; Zhang, J.; Feng, X.; Shen, J.; Zhang, Z.; Guo, M.; Li, K.; Ou, Y.; Wei, P.; Wang, L.-L.; Ji, Z.-Q.; Feng, Y.; Ji, S.; Chen, X.; Jia, J.; Dai, X.; Fang, Z.; Zhang, S.-C.; He, K.; Wang, Y.; Lu, L.; Ma, X.-C.; Xue, Q.-K. Experimental Observation of the Quantum Anomalous Hall Effect in a Magnetic Topological Insulator. *Science* 2013, 340 (6129), 167.
- (9) Wang, Z.; Gutiérrez-Lezama, I.; Ubrig, N.; Kroner, M.; Gibertini, M.; Taniguchi, T.; Watanabe, K.; Imamoğlu, A.; Giannini, E.; Morpurgo, A. F. Very Large Tunneling Magnetoresistance in Layered Magnetic Semiconductor CrI3. *Nat. Commun.* **2018**, *9* (1), 2516.
- (10) Cai, X.; Song, T.; Wilson, N. P.; Clark, G.; He, M.; Zhang, X.; Taniguchi, T.; Watanabe, K.; Yao, W.; Xiao, D.; McGuire, M. A.; Cobden, D. H.; Xu, X. Atomically Thin CrCl3: An In-Plane Layered Antiferromagnetic Insulator. *Nano Lett.* **2019**, *19* (6), 3993–3998.

- (11) Abramchuk, M.; Jaszewski, S.; Metz, K. R.; Osterhoudt, G. B.; Wang, Y.; Burch, K. S.; Tafti, F. Controlling Magnetic and Optical Properties of the van der Waals Crystal CrCl3–xBrx *via* Mixed Halide Chemistry. *Adv. Mater.* **2018**, *30* (25), 1801325.
- (12) Richter, N.; Weber, D.; Martin, F.; Singh, N.; Schwingenschlögl, U.; Lotsch, B. V.; Kläui, M. Temperature-Dependent Magnetic Anisotropy in the Layered Magnetic Semi-conductors CrI3 and CrBr3. *Phys. Rev. Mater.* **2018**, 2 (2), 024004.
- (13) Yu, X.; Zhang, X.; Shi, Q.; Tian, S.; Lei, H.; Xu, K.; Hosono, H. Large Magnetocaloric Effect in van der Waals Crystal CrBr3. Front. Phys. 2019, 14 (4), 43501.
- (14) McGuire, M. A.; Dixit, H.; Cooper, V. R.; Sales, B. C. Coupling of Crystal Structure and Magnetism in the Layered, Ferromagnetic Insulator CrI3. *Chem. Mater.* **2015**, *27* (2), 612–620.
- (15) Shcherbakov, D.; Stepanov, P.; Weber, D.; Wang, Y.; Hu, J.; Zhu, Y.; Watanabe, K.; Taniguchi, T.; Mao, Z.; Windl, W.; Goldberger, J.; Bockrath, M.; Lau, C. N. Raman Spectroscopy, Photocatalytic Degradation, and Stabilization of Atomically Thin Chromium Tri-iodide. *Nano Lett.* **2018**, *18* (7), 4214–4219.
- (16) Sun, X.; Li, W.; Wang, X.; Sui, Q.; Zhang, T.; Wang, Z.; Liu, L.; Li, D.; Feng, S.; Zhong, S.; Wang, H.; Bouchiat, V.; Nunez Regueiro, M.; Rougemaille, N.; Coraux, J.; Purbawati, A.; Hadj-Azzem, A.; Wang, Z.; Dong, B.; Wu, X.; Yang, T.; Yu, G.; Wang, B.; Han, Z.; Han, X.; Zhang, Z. Room Temperature Ferromagnetism in Ultra-Thin van der Waals Crystals of 1T-CrTe2. *Nano Res.* **2020**, *13* (12), 3358–3363.
- (17) Meng, L.; Zhou, Z.; Xu, M.; Yang, S.; Si, K.; Liu, L.; Wang, X.; Jiang, H.; Li, B.; Qin, P.; Zhang, P.; Wang, J.; Liu, Z.; Tang, P.; Ye, Y.; Zhou, W.; Bao, L.; Gao, H.-J.; Gong, Y. Anomalous Thickness Dependence of Curie Temperature in Air-Stable Two-Dimensional Ferromagnetic 1T-CrTe2 Grown by Chemical Vapor Deposition. *Nat. Commun.* 2021, 12 (1), 809.
- (18) Zhang, X.; Lu, Q.; Liu, W.; Niu, W.; Sun, J.; Cook, J.; Vaninger, M.; Miceli, P. F.; Singh, D. J.; Lian, S.-W.; Chang, T.-R.; He, X.; Du, J.; He, L.; Zhang, R.; Bian, G.; Xu, Y. Room-Temperature Intrinsic Ferromagnetism in Epitaxial CrTe2 Ultrathin Films. *Nat. Commun.* **2021**, *12* (1), 2492.
- (19) Freitas, D. C.; Núñez, M.; Strobel, P.; Sulpice, A.; Weht, R.; Aligia, A. A.; Núñez-Regueiro, M. Antiferromagnetism and Ferromagnetism in Layered 1T-CrSe2 with V and Ti Replacements. *Phys. Rev. B* **2013**, *87* (1), 014420.
- (20) Li, B.; Wan, Z.; Wang, C.; Chen, P.; Huang, B.; Cheng, X.; Qian, Q.; Li, J.; Zhang, Z.; Sun, G.; Zhao, B.; Ma, H.; Wu, R.; Wei, Z.; Liu, Y.; Liao, L.; Ye, Y.; Huang, Y.; Xu, X.; Duan, X.; Ji, W.; Duan, X. Van der Waals Epitaxial Growth of Air-Stable CrSe2 Nanosheets with Thickness-Tunable Magnetic Order. *Nat. Mater.* 2021, 20 (6), 818–825
- (21) Li, Q.; Zhao, X.; Deng, L.; Shi, Z.; Liu, S.; Wei, Q.; Zhang, L.; Cheng, Y.; Zhang, L.; Lu, H.; Gao, W.; Huang, W.; Qiu, C.-W.; Xiang, G.; Pennycook, S. J.; Xiong, Q.; Loh, K. P.; Peng, B. Enhanced Valley Zeeman Splitting in Fe-Doped Monolayer MoS2. ACS Nano 2020, 14 (4), 4636–4645.
- (22) Tan, H.; Wang, C.; Hu, W.; Duan, H.; Guo, P.; Li, N.; Li, G.; Cai, L.; Sun, Z.; Hu, F.; Yan, W. Reversible Tuning of the Ferromagnetic Behavior in Mn-Doped MoS2 Nanosheets *via* Interface Charge Transfer. *ACS Appl. Mater. Interfaces* **2018**, 10 (37), 31648–31654.
- (23) Martinez, L. M.; Delgado, J. A.; Saiz, C. L.; Cosio, A.; Wu, Y.; Villagrán, D.; Gandha, K.; Karthik, C.; Nlebedim, I. C.; Singamaneni, S. R. Magnetic and Electrocatalytic Properties of Transition Metal Doped MoS2 Nanocrystals. *J. Appl. Phys.* **2018**, *124* (15), 153903.
- (24) Dau, M. T.; Vergnaud, C.; Gay, M.; Alvarez, C. J.; Marty, A.; Beigné, C.; Jalabert, D.; Jacquot, J. F.; Renault, O.; Okuno, H.; Jamet, M. Van der Waals Epitaxy of Mn-Doped MoSe2 on Mica. *APL Mater.* **2019**, *7* (5), 051111.
- (25) Zhang, F.; Zheng, B.; Sebastian, A.; Olson, D. H.; Liu, M.; Fujisawa, K.; Pham, Y. T. H.; Jimenez, V. O.; Kalappattil, V.; Miao, L.; Zhang, T.; Pendurthi, R.; Lei, Y.; Elías, A. L.; Wang, Y.; Alem, N.; Hopkins, P. E.; Das, S.; Crespi, V. H.; Phan, M.-H.; Terrones, M.

- Monolayer Vanadium-Doped Tungsten Disulfide: A Room-Temperature Dilute Magnetic Semiconductor. *Adv. Sci.* **2020**, 7 (24), 2001174.
- (26) Pham, Y. T. H.; Liu, M.; Jimenez, V. O.; Yu, Z.; Kalappattil, V.; Zhang, F.; Wang, K.; Williams, T.; Terrones, M.; Phan, M.-H. Tunable Ferromagnetism and Thermally Induced Spin Flip in Vanadium-Doped Tungsten Diselenide Monolayers at Room Temperature. *Adv. Mater.* **2020**, *32* (45), 2003607.
- (27) Kepp, K. P. A Quantitative Scale of Oxophilicity and Thiophilicity. *Inorg. Chem.* **2016**, *55* (18), 9461–9470.
- (28) Pi, L.; Li, L.; Liu, K.; Zhang, Q.; Li, H.; Zhai, T. Recent Progress on 2D Noble-Transition-Metal Dichalcogenides. *Adv. Funct. Mater.* **2019**, 29 (51), 1904932.
- (29) Wang, Z.; Li, Q.; Besenbacher, F.; Dong, M. Facile Synthesis of Single Crystal PtSe2 Nanosheets for Nanoscale Electronics. *Adv. Mater.* **2016**, 28 (46), 10224–10229.
- (30) Wang, Y.; Li, L.; Yao, W.; Song, S.; Sun, J. T.; Pan, J.; Ren, X.; Li, C.; Okunishi, E.; Wang, Y.-Q.; Wang, E.; Shao, Y.; Zhang, Y. Y.; Yang, H.-t.; Schwier, E. F.; Iwasawa, H.; Shimada, K.; Taniguchi, M.; Cheng, Z.; Zhou, S.; Du, S.; Pennycook, S. J.; Pantelides, S. T.; Gao, H.-J. Monolayer PtSe2, a New Semiconducting Transition-Metal-Dichalcogenide, Epitaxially Grown by Direct Selenization of Pt. *Nano Lett.* 2015, 15 (6), 4013–4018.
- (31) Zhao, Y.; Qiao, J.; Yu, P.; Hu, Z.; Lin, Z.; Lau, S. P.; Liu, Z.; Ji, W.; Chai, Y. Extraordinarily Strong Interlayer Interaction in 2D Layered PtS2. Adv. Mater. 2016, 28 (12), 2399–2407.
- (32) Zhao, Y.; Qiao, J.; Yu, Z.; Yu, P.; Xu, K.; Lau, S. P.; Zhou, W.; Liu, Z.; Wang, X.; Ji, W.; Chai, Y. High-Electron-Mobility and Air-Stable 2D Layered PtSe2 FETs. *Adv. Mater.* **2017**, *29* (5), 1604230.
- (33) Oyedele, A. D.; Yang, S.; Liang, L.; Puretzky, A. A.; Wang, K.; Zhang, J.; Yu, P.; Pudasaini, P. R.; Ghosh, A. W.; Liu, Z.; Rouleau, C. M.; Sumpter, B. G.; Chisholm, M. F.; Zhou, W.; Rack, P. D.; Geohegan, D. B.; Xiao, K. PdSe2: Pentagonal Two-Dimensional Layers with High Air Stability for Electronics. *J. Am. Chem. Soc.* **2017**, 139 (40), 14090–14097.
- (34) Ma, H.; Chen, P.; Li, B.; Li, J.; Ai, R.; Zhang, Z.; Sun, G.; Yao, K.; Lin, Z.; Zhao, B.; Wu, R.; Tang, X.; Duan, X.; Duan, X. Thickness-Tunable Synthesis of Ultrathin Type-II Dirac Semimetal PtTe2 Single Crystals and Their Thickness-Dependent Electronic Properties. *Nano Lett.* **2018**, *18* (6), 3523–3529.
- (35) Xu, H.; Wei, J.; Zhou, H.; Feng, J.; Xu, T.; Du, H.; He, C.; Huang, Y.; Zhang, J.; Liu, Y.; Wu, H.-C.; Guo, C.; Wang, X.; Guang, Y.; Wei, H.; Peng, Y.; Jiang, W.; Yu, G.; Han, X. High Spin Hall Conductivity in Large-Area Type-II Dirac Semimetal PtTe2. Adv. Mater. 2020, 32 (17), 2000513.
- (36) Wilson, J. A.; Yoffe, A. D. The Transition Metal Dichalcogenides Discussion and Interpretation of the Observed Optical, Electrical and Structural Properties. *Adv. Phys.* **1969**, *18* (73), 193–335.
- (37) Liu, Y.; Petrovic, C. Critical Behavior of the Quasi-Two-Dimensional Weak Itinerant Ferromagnet Trigonal Chromium Telluride Cr0.62Te. *Phys. Rev. B* **2017**, *96* (13), 134410.
- (38) McGuire, M. A.; Garlea, V. O.; Kc, S.; Cooper, V. R.; Yan, J.; Cao, H.; Sales, B. C. Antiferromagnetism in the van der Waals Layered Spin-Lozenge Semiconductor CrTe3. *Phys. Rev. B* **2017**, *95* (14), 144421.
- (39) Wen, Y.; Liu, Z.; Zhang, Y.; Xia, C.; Zhai, B.; Zhang, X.; Zhai, G.; Shen, C.; He, P.; Cheng, R.; Yin, L.; Yao, Y.; Getaye Sendeku, M.; Wang, Z.; Ye, X.; Liu, C.; Jiang, C.; Shan, C.; Long, Y.; He, J. Tunable Room-Temperature Ferromagnetism in Two-Dimensional Cr2Te3. *Nano Lett.* **2020**, 20 (5), 3130–3139.
- (40) Lukoschus, K.; Kraschinski, S.; Näther, C.; Bensch, W.; Kremer, R. K. Magnetic Properties and Low Temperature X-ray Studies of the Weak Ferromagnetic Monoclinic and Trigonal Chromium Tellurides Cr5Te8. *J. Solid State Chem.* **2004**, *177* (3), 951–959.
- (41) Luo, X.-H.; Ren, W.-J.; Zhang, Z.-D. Magnetic Properties and Magnetocaloric Effect of a Trigonal Te-Rich Cr5Te8 Single Crystal. *J. Magn. Magn. Mater.* **2018**, *445*, 37–43.

- (42) Zhang, L.-Z.; He, X.-D.; Zhang, A.-L.; Xiao, Q.-L.; Lu, W.-L.; Chen, F.; Feng, Z.; Cao, S.; Zhang, J.; Ge, J.-Y. Tunable Curie Temperature in Layered Ferromagnetic Cr5+xTe8 Single Crystals. *APL Mater.* **2020**, *8* (3), 031101.
- (43) Foner, S. High-Field Antiferromagnetic Resonance in Cr2O3. *Phys. Rev.* **1963**, *130* (1), 183–197.
- (44) Rhodes, P.; Wohlfarth, E. P.; Jones, H. The Effective Curie-Weiss Constant of Ferromagnetic Metals and Alloys. *Proc. R. Soc. London, Ser. A* 1963, 273 (1353), 247–258.
- (45) May, A. F.; Calder, S.; Cantoni, C.; Cao, H.; McGuire, M. A. Magnetic Structure and Phase Stability of the van der Waals Bonded Ferromagnet Fe3-xGeTe2. *Phys. Rev. B* **2016**, *93* (1), 014411.
- (46) Wohlfarth, E. P. Magnetic Properties of Crystalline and Amorphous Alloys: A Systematic Discussion Based on the Rhodes-Wohlfarth Plot. J. Magn. Magn. Mater. 1978, 7 (1), 113–120.
- (47) Moriya, T. Recent Progress in the Theory of Itinerant Electron Magnetism. J. Magn. Magn. Mater. 1979, 14 (1), 1–46.
- (48) Buschow, K. H. J.; de Boer, F. R., Itinerant-Electron Magnetism. In *Physics of Magnetism and Magnetic Materials*; Springer US: Boston, MA, 2003; pp 63–73.
- (49) Milenov, T. I.; Tenev, T.; Miloushev, I.; Avdeev, G. V.; Luo, C. W.; Chou, W. C. Preliminary Studies of the Raman Spectra of Ag2Te and Ag5Te3. Opt Quantum Electron. 2014, 46, 573–580.
- (50) van de Walle, A.; Tiwary, P.; de Jong, M.; Olmsted, D. L.; Asta, M.; Dick, A.; Shin, D.; Wang, Y.; Chen, L. Q.; Liu, Z. K. Efficient Stochastic Generation of Special Quasirandom Structures. *Calphad* **2013**, *42*, 13–18.
- (51) Zunger, A.; Wei, S. H.; Ferreira, L. G.; Bernard, J. E. Special Quasirandom Structures. *Phys. Rev. Lett.* **1990**, *65* (3), 353–356.
- (52) Kresse, G.; Furthmüller, J. Efficient Iterative Schemes for *ab Initio* Total-Energy Calculations Using a Plane-Wave Basis Set. *Phys. Rev. B* **1996**, 54 (16), 11169–11186.
- (53) Blöchl, P. E. Projector Augmented-Wave Method. *Phys. Rev. B* **1994**, 50 (24), 17953–17979.
- (54) Perdew, J. P.; Burke, K.; Ernzerhof, M. Generalized Gradient Approximation Made Simple. *Phys. Rev. Lett.* **1996**, 77 (18), 3865–3868.
- (55) Tkatchenko, A.; DiStasio, R. A.; Car, R.; Scheffler, M. Accurate and Efficient Method for Many-Body van der Waals Interactions. *Phys. Rev. Lett.* **2012**, *108* (23), 236402.
- (56) Grimme, S. Semiempirical GGA-type Density Functional Constructed with a Long-Range Dispersion Correction. *J. Comput. Chem.* **2006**, 27 (15), 1787–1799.